Acta Pharmaceutica Sinica B 2025;15(3):1242−1254

Chinese Pharmaceutical Association
Institute of Materia Medica, Chinese Academy of Medical Sciences

Acta Pharmaceutica Sinica B

www.elsevier.com/locate/apsb
www.sciencedirect.com

ORIGINAL ARTICLE

Remodeling tumor immunosuppressive microenvironment through dual activation of immunogenic panoptosis and ferroptosis by H_2S-amplified nanoformulation to enhance cancer immunotherapy

Yingli Luo[a,c,†], Maoyuan Linghu[a,†], Xianyu Luo[a], Dongdong Li[d], Jilong Wang[d], Shaojun Peng[b,*], Yinchu Ma[a,c,*]

[a]*Wuxi School of Medicine, Jiangnan University, Wuxi 214122, China*
[b]*Center for Biological Science and Technology & College of Arts and Sciences, Beijing Normal University, Zhuhai 519087, China*
[c]*Affiliated Hospital of Jiangnan University, Jiangnan University, Wuxi 214062, China*
[d]*Joint Centre of Translational Medicine, Wenzhou Institute, University of Chinese Academy of Sciences, Wenzhou 325000, China*

Received 28 August 2024; received in revised form 29 November 2024; accepted 5 December 2024

KEY WORDS

PANoptosis;
Ferroptosis;
Nanomedicine;
H_2S gas therapy;
Immunogenic cell death;
Remodeling immunosuppressive microenvironment;

Abstract The deficiency in immunogenicity and the presence of immunosuppression within the tumor microenvironment significantly hindered the efficacy of immunotherapy. Consequently, a nanoformulation containing metal sulfide of FeS and GSDMD plasmid ($NP_{FeS/GD}$) had been developed to effectively augment antitumor immune responses through dual activation of immunogenic PANoptosis and ferroptosis, as well as reprogramming immunosuppressive effects *via* H_2S amplification. The bioactive $NP_{FeS/GD}$ exhibited controlled release of GSDMD plasmid, H_2S, and Fe^{2+} in response to the tumor microenvironment. Fe^{2+}, H_2S, and the expression of GSDMD protein could effectively elicit highly immunogenic PANoptosis and ferroptosis. Furthermore, releasing H_2S could mitigate the overexpression of indoleamine 2,3-dioxygenase1 (IDO1) induced by immunogenic PANoptotic and ferroptotic cell death and disrupt the

*Corresponding authors.
E-mail addresses: 91122024006@bnu.edu.cn (Shaojun Peng), 91122024006@bnu.edu.cn, myc2022@jiangnan.edu.cn (Yinchu Ma).
[†]These authors made equal contributions to this work.
Peer review under the responsibility of Chinese Pharmaceutical Association and Institute of Materia Medica, Chinese Academy of Medical Sciences.

https://doi.org/10.1016/j.apsb.2024.12.014

Cancer immunotherapy;
Metastasis prevention

activity of IDO1. Consequently, $NP_{FeS/GD}$ effectively triggered the antitumor innate and adaptive immune responses through induction of PANoptotic and ferroptotic cell death and reshaped the tumor immunosuppressive microenvironment to enhance antitumor immunotherapy for metastasis inhibition. This study unveiled the significant potential of immunogenic PANoptosis and ferroptosis in H_2S gas therapy for enhancing tumor immunotherapy, offering novel insights and ideas for the rational design of nanomedicine to enhance tumor immunogenicity while reprogramming the tumor immunosuppressive microenvironment.

1. Introduction

Antitumor immunotherapies have emerged as a promising new cornerstone in therapeutic oncology, effectively leveraging the body's immune system to combat tumors by overcoming tumor-induced immunosuppression and precisely recognizing and destroying tumor cells[1-5]. However, challenges arise from poor immunogenicity and a robust tumor immunosuppressive microenvironment, posing difficulties in achieving durable response rates for cancer treatment through immune system activation[6-8]. On the one hand, the infiltration of lymphocytes at the tumor site may be constrained by multiple immunosuppressive mechanisms, including the inhibition of regulatory T cells (Tregs) and the induced expression of inhibitory checkpoint receptors[9-11]. Cancer cells with high mutation rates can also generate neoantigens that hinder recognition by dendritic cells (DCs) or result in poor recognition, leading to immune evasion[12]. Moreover, the acidic and hypoxic characteristics of the tumor microenvironment contribute to reduced lymphocyte infiltration and enhanced immune escape, thereby impacting the efficacy of tumor immunotherapy[13-15]. Therefore, to achieve effective cancer immunotherapy, it is imperative to strengthen neoantigen production to improve tumor immunogenicity and reprogram tumor immunosuppression to augment immune response rates[16-18].

Currently, a new thread is emerging regarding the external perspective on how immunogenic PANoptosis and ferroptosis of cancer cells induce immunogenicity to influence the tumor immune microenvironment[19-22]. Specifically, this evidence pertains to the inflammatory cell death of PANoptosis and ferroptosis. Ferroptosis, a form of iron-dependent cell death, is characterized by the accumulation of lethal levels of iron-dependent lipid peroxides in cells, resulting in oxidative stress, mitochondrial damage, and cell membrane rupture, ultimately leading to non-apoptotic death[23-25]. PANoptosis represents an inflammation-regulated cell death pathway that exhibits critical features of pyroptosis, necroptosis, and apoptosis simultaneously[26-28], while ferroptosis is an iron-dependent, non-apoptotic form of regulated cell death. Both PANoptosis and ferroptosis can induce immunogenic cell death (ICD), leading to the release of tumor-associated antigens (TAAs) and damage-associated molecular patterns (DAMPs) from dying tumor cells, thereby triggering a robust and sustained tumor-specific immunological response[19,21,29-34]. The combination of PANoptosis and ferroptosis can synergistically enhance tumor immunogenicity, thereby improving the efficacy of cancer immunotherapy. The interaction between these cell death pathways can lead to the release of a vast array of tumor antigens, which can be presented by dendritic cells to activate T cells[35,36]. This increased antigen presentation can stimulate a more robust anti-tumor immune response. Furthermore, the metabolic changes and oxidative stress induced by PANoptosis and ferroptosis can create an immunogenic tumor microenvironment, promoting the recruitment and activation of immune cells. In addition, these cell death pathways can modulate the balance between pro-inflammatory and anti-inflammatory cytokines, tipping the scales in favor of an immune response detrimental to tumor growth.

Nevertheless, the process of inflammatory cell death, while enhancing tumor immunogenicity, also serves as a double-edged sword by activating the immunosuppressive microenvironment of the tumor and thereby attenuating the anti-tumor immune responses[37-41]. ICD stimulates effector T cells to secrete interferon-γ (IFN-γ), which in turn induces the transcriptional activation of the indoleamine 2,3-dioxygenase1 (IDO1) promoter, resulting in an increased expression of IDO1 in tumor cells and DCs. Elevated levels of IDO1 can deplete the enzyme responsible for converting tryptophan into excessive kynurenine, leading to the adoption of an immunosuppressive phenotype by DCs and promoting the differentiation of Tregs, thereby enhancing the immunosuppressive microenvironment within tumors as a negative regulatory response[42-46].

Hydrogen sulfide (H_2S) is an endogenously produced gaseous signaling molecule present in mammals that significantly influences tumorigenesis[47,48]. Metabolic and signaling pathway disparities between malignant and non-malignant cells may disturb the redox balance within tumor cells by elevating exogenous H_2S levels, predominantly through mitochondrial dysfunction, resulting in cellular "chemical asphyxiation", thereby triggering the release of DAMPs through activation of tumor danger signal transduction pathways[49-52]. Previous studies have shown that H_2S can reduce the expression of IDO1 by inhibiting the NF-κB and STAT3 pathways, and disrupting IDO1 activity through H_2S/NO crosstalk[53-55]. The results show a reduction in tryptophan metabolism and kynurenine production, the promotion of T effector cells, and the inhibition of the immunosuppressive microenvironment. Ultimately, this leads to an enhanced efficacy of cancer immunotherapy.

In this study, we have developed a tumor-targeted nanoformulation containing metal sulfide of FeS and GSDMD plasmid ($NP_{FeS/GD}$) with PANoptosis/ferroptosis-inducing capabilities. The aim is to achieve increased tumor immunogenicity and reprogram the tumor immunosuppressive microenvironment, thereby enhancing antitumor immunotherapy efficacy and inhibiting metastasis (Fig. 1). The obtained $NP_{FeS/GD}$ demonstrates excellent physiological stability and exhibits controlled release of GSDMD plasmid, H_2S, and Fe^{2+} in response to the tumor microenvironment. The release of H_2S, along with the expression of the GSDMD protein from the released plasmid, triggers a highly immunogenic form of PANoptotic cell death, encompassing pyroptosis, necroptosis, and apoptosis. The released Fe^{2+} can

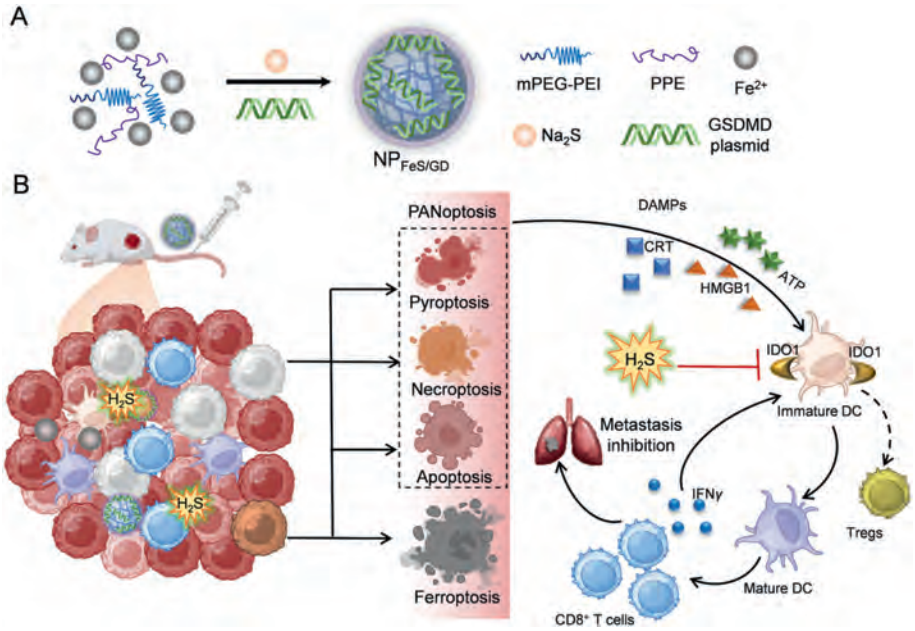

Figure 1 Schematic illustration showing the (A) preparation of $NP_{FeS/GD}$ and (B) its ability to trigger PANoptotic and ferroptotic cell death, leading to immunosuppressive remodeling for improved antitumor immunotherapy and inhibition of metastasis. Some graphical elements created by biorender.com.

effectively trigger oxidative stress, leading to the generation of ROS and the inhibition of Glutathione Peroxidase 4 (GPX4), ultimately promoting ferroptosis. Additionally, the released H_2S can reduce the excessive expression of IDO1 caused by immunogenic PANoptosis and ferroptosis cell death, ultimately inhibiting the activity of IDO1. Consequently, $NP_{FeS/GD}$ effectively triggers the antitumor innate and adaptive immune responses through induction of PANoptotic and ferroptotic cell death and reshapes the tumor immunosuppressive microenvironment to enhance antitumor immunotherapy for inhibiting metastasis.

2. Materials and methods

2.1. Materials

The plasmid GSDMD was obtained from TSINGKE Biological Technology (Guangzhou, China). Lipofectamine 3000 Transfection Reagent was purchased from Thermo Fisher (Waltham, MA, USA). Methoxy polyethylene glycol-*g*-polyethyleneimine ($mPEG_{5k}$-*g*-PEI_{25k}) was bought from Tanshtech Co., Ltd. (Guangzhou, China). Cy5-NHS was purchased from Meilunbio (MB12193, Dalian, China). Iron (II) chloride ($FeCl_2$), Na_2S, and WSP-1 were purchased from Shanghai Macklin Biochemical Technology Co., Ltd. (Shanghai, China). 4′,6-Diamidine-2′-phenylindole dihydrochloride (DAPI), collagenase I, and IV were obtained from Sigma−Aldrich (Saint Louis, and MO, USA). LDC7559 (BD01225006) and Necrostatin-1 (BD14657) were bought from Bidepharm (Shanghai, China). Z-VAD-FMK (JX517845) was obtained from Energy Chemical (Shanghai, China). Ferrostatin-1 (HY-100579) was purchased from MedChem Express LLC. (Monmouth Junction, and NJ, USA). Apoptosis and Necrosis Detection Kit with YO-PRO-1 and PI (YP1/PI) was bought from Beyotime Biotechnology (Shanghai, China). NF-κB p65 Antibody (T55034), Phospho-NF-κB p65 (Ser536) Antibody (TA2006), STAT3 Antibody (T55292), Phospho-STAT3 (Y705) Antibody (T56566), Calreticulin Antibody (T55353), GPX4 Antibody (T56959), HMGB1 Antibody (T55060), Phospho-MLKL Antibody (*p*-MLKL, TA7420), total and cleaved N-terminal GSDMD Antibody (P30823) and caspase-3 Antibody (TA6311) were purchased from Abmart (Shanghai, China). Indoleamine 2,3-dioxygenase Antibody (IDO1, ab277522), Donkey Anti-Rabbit IgG H&L (Alexa Fluor® 488) (ab150073), and Donkey Anti-Rabbit IgG H&L (Alexa Fluor® 568) (ab175470) were bought from Abcam (Shanghai, China). ELISA kits of TNF-α, IL-6, and IFN-γ were purchased from DAKEWE (Shenzhen, China). ATP assay kit (S0027) was purchased from Beyotime Biotechnology (Shanghai, China). The flow cytometry antibodies (anti-CD16/32, BV510-conjugated anti-CD45, BV421 anti-mouse CD3, PE-Cy7 anti-mouse CD4, BV650 anti-mouse CD8, PE anti-mouse Foxp3, FITC anti-mouse CD44, PerCP-Cy5.5 anti-mouse CD11c, PE anti-mouse CD62L, Alexa Fluor® 488 anti-mouse CD80, and APC/Cy7 anti-mouse CD86) were purchased from Biolegend (San Diego, CA, USA).

2.2. Preparation and characterization of the nanocomplex of FeS and GSDMD plasmid ($NP_{FeS/GD}$)

At first, 1.0 mL of $FeCl_2$ aqueous solution (1.0 mmol/L), 1.0 mL of PPE aqueous solution (10 mg/mL), and 1.0 mL of $mPEG_{5k}$-PEI_{25k} (0, 0.1, 0.2, 0.5 and 1.0 mg/mL) were mixed with stirring in a flask at 25 °C for 0.5 h. Then, 0.2 mL of an aqueous solution containing Na_2S (1.0 mmol/L) and GSDMD plasmid (0.1 mg/mL) was added dropwise for another 0.5 h. After the reaction, the mixed solution was dialyzed in pure water overnight, and the samples collected after dialysis were concentrated in an ultrafiltration tube and centrifuged at 3000 rpm (Sorvall Legend Micro 17 Centrifuge, ThermoScientific, Germany) for 5 min to collect the supernatant. The NP_{FeS} was prepared using the method mentioned above without the GSDMD plasmid. The NP_{GD} was constructed without the use of $FeCl_2$ and Na_2S. The $NP_{FeS/GD\text{-}Cy5}$ was prepared

using the abovementioned method, with Cy5-NHS (0.2 mg) added for conjugation with mPEG-PEI. The zeta potential and size distribution of the nanocomplex were detected by dynamic light scattering (DLS, Zetasizer, and Nano ZS90, Worcestershire, UK). The morphology and mapping analysis of the nanocomplex were obtained using a transmission electron microscope (TEM, JEM-2011, JEOL, Japan).

2.3. Analysis of cell death patterns

NP_{GD}, NP_{FeS}, and $NP_{FeS/GD}$ (20 μg/mL with 1.0 μg/mL of plasmid) were co-incubated with 4T1 cells in 12-well plates for 12 h. The cells were collected and stained with YP1/PI staining kits to analyze the types of cell death. Meanwhile, the expression of key proteins *p*-MLKL, GSDMD, and caspase-3 related to cell death patterns was analyzed by immunoblotting and CLSM. Apoptotic cells demonstrated green fluorescence; necroptotic cells showed red or green fluorescence; pyroptotic cells displayed red fluorescence; and PANopototic cells exhibited yellow fluorescence.

2.4. Analysis of immunogenic cell death in vitro

To verify the ability of different formulations to induce immunogenic cell death (ICD) *in vitro*, the release of high mobility group box 1 (HMGB1), secretion of adenosine triphosphate (ATP), and exposure of calreticulin (CRT) were examined. NP_{GD}, NP_{FeS}, and $NP_{FeS/GD}$ (20 μg/mL with 1.0 μg/mL plasmid) were co-incubated with 4T1 cells in 12-well plates for 12 h. The extracellular ATP secreted from the cells in the medium was measured using an ATP bioluminescent assay kit. The cells were collected and stained with 4% paraformaldehyde (PFA, Macklin). After being washed three times with PBS, the cells were incubated with CRT and HMGB1 antibodies (ICD markers). The exposure of CRT and release of HMGB1 were measured using CLSM.

2.5. In vivo antitumor efficacy

All experimental procedures were executed according to the protocols approved by the Jiangnan University Animal Care and Use Committee (JN. No20231115b0980531[544]). 4T1 tumor-bearing mice were intravenously injected with PBS, NP_{GD}, NP_{FeS}, and $NP_{FeS/GD}$ (5 mg/kg with 1.0 mg/kg plasmid) on Days 10,13, and 16. The tumor volume and mouse body weight were recorded every 3 days. On Day 22, the spleens, tumor-draining lymph nodes, and tumors of the tumor-bearing mice were collected to obtain the isolated immune cells following a previous study. The cells were stained with antibodies to measure the proportion of CD8 T cells, Treg cells, and memory T cells using FACS. More detailed experimental details are included in the Supporting Information

3. Results and discussion

3.1. Preparation and characterization and cellular uptake of multifunctional nanoformulation

To prepare the nanocomplex of $NP_{FeS/GD}$ for inducing immunogenic PANoptosis and ferroptosis, biocompatible polyphosphate ester (PPE, ^{1}H NMR was shown in Supporting Information Fig. S1) and $mPEG_{5k}$-PEI_{25k} were synthesized to stabilize the nanomedicine structures during the construction of FeS nanoparticles (NP_{FeS}) and to facilitate the binding of gasdermin D (GSDMD) plasmid. The hydrophilic polymer PPE could provide a hydration layer to the nanocomplex to protect the FeS core from oxidation. As shown in Supporting Information Fig. S2, when the polymer PPE was not present during the $NP_{FeS/GD}$ preparation process, the obtained nanocomplex was highly unstable, leading to oxidative aggregation and precipitation of the nanocomplex within a short period. Firstly, the expression of GSDMD proteins in the engineered vehicles was successfully verified by immunoblot analysis (Supporting Information Fig. S3). The binding efficiency of the GSDMD plasmid and NP_{FeS} was obtained through electrophoresis. The nanocomplex of NP_{FeS} could effectively bind the GSDMD plasmid through electrostatic interactions when the weight ratio between the cationic $mPEG_{5k}$-PEI_{25k} and the plasmid was 5 or higher (Fig. 2A). As the weight ratios increased, the zeta potentials of the nanocomplexes also increased (Fig. 2B). Therefore, the $mPEG_{5k}$-PEI_{25k} and GSDMD plasmid were chosen with a weight ratio of 5 to form a nanocomplex in the following experiments, known as $NP_{FeS/GD}$. The size distribution and zeta potential of the NP_{FeS} were approximately 190 nm and 18 mV. Meanwhile, after binding the GSDMD plasmid to NP_{FeS}, the size distribution and zeta potential of $NP_{FeS/GD}$ were approximately 220 nm and −0.45 mV. As a control, when the $mPEG_{5k}$-PEI_{25k} and GSDMD plasmid were combined without FeS to form NP_{GD}, the size distribution and zeta potential of NP_{GD} were approximately 230 nm and 1.60 mV (Fig. 2C and Supporting Information Fig. S4). Following a 24 h incubation with PBS buffer (pH 7.4), the sizes of NP_{FeS} and $NP_{FeS/GD}$ showed minimal changes, indicating their excellent stability (Supporting Information Fig. S5). The results indicated that the neutral-charged PPE played a crucial role in stabilizing the NP_{FeS} structures and preventing aggregation, forming stable nanocomplexes capable of efficiently delivering the GSDMD plasmid. The morphology and composition of NP_{FeS} and $NP_{FeS/GD}$ were measured by transmission electron microscopy (TEM). As shown in Fig. 2D, the NP_{FeS} and $NP_{FeS/GD}$ structures displayed consistent morphologies. Analysis of the mapping data revealed a uniform distribution of Fe and S elements within the nanocomplex. In PBS buffer at pH 7.4 and 6.8, the measurement of Fe^{2+} released from $NP_{FeS/GD}$ was conducted. It was observed that 98.2% and 84.8% of $NP_{FeS/GD}$ degraded in the acidic PBS buffer at pH 5.0 and 6.8, while only 68.3% of Fe^{2+} was released at pH 7.4 (Fig. 2E and Supporting Information Fig. S6). Additionally, the released H_2S content from $NP_{FeS/GD}$ in the acidic solution reached up to 86.9% after 5 h of incubation, which was significantly higher compared to the release in PBS at pH 7.4 (Fig. 2F). The $NP_{FeS/GD}$ nanocomplex was able to effectively respond to the acidic tumor microenvironment, leading to the release of Fe^{2+} and H_2S. This pH-responsive behavior was crucial for targeted drug delivery and therapeutic efficacy. Overall, the results confirmed the successful synthesis and characterization of the $NP_{FeS/GD}$ nanocomplex, which possessed desirable stability and pH-responsiveness.

To investigate the intracellular uptake of the prepared nanocomplex, confocal laser scanning microscopy (CLSM) was performed. The fluorescent signal was observed after incubation with $NP_{FeS/GD\text{-}Cy5}$ for different times (2, 4, and 8 h). As shown in Fig. 2G and H, the mean fluorescence intensity (MFI) of Cy5 in cells increased gradually with longer incubation times. However, there was no notable difference in the Cy5 signal between 4 and 8 h of incubation. This indicated that the $NP_{FeS/GD}$ nanocomplex was efficiently internalized by the cells within the first 4 h, and the uptake reached a plateau after 8 h. Then the Fe content in the cells was measured after incubation with $NP_{FeS/GD}$ at different times (2,

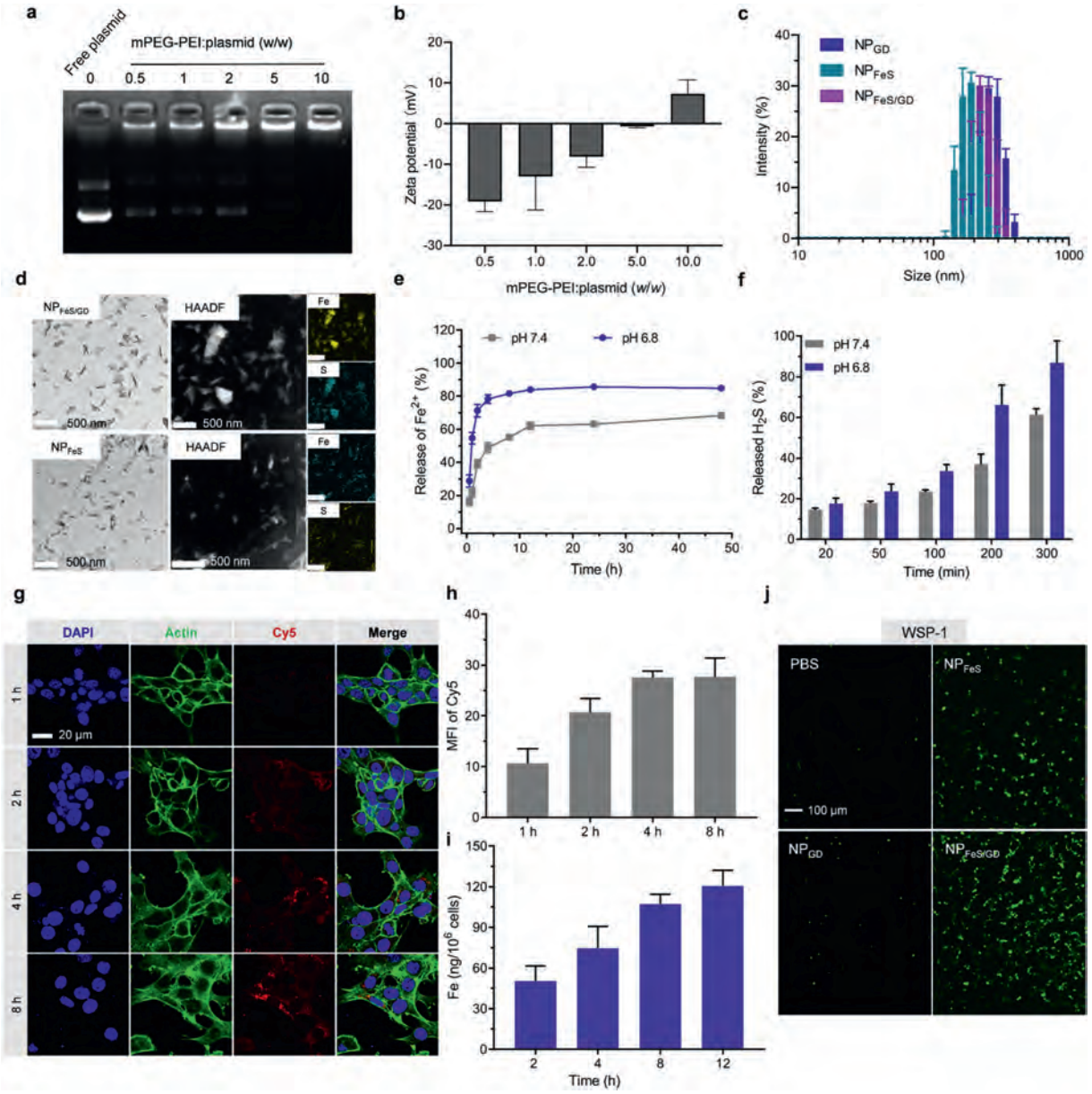

Figure 2 (A) Agarose gel electrophoresis of GSDMD plasmid and mPEG-PEI at different weight ratios. (B) Zeta potential of the formed nanoformulation $NP_{FeS/GD}$ of mPEG-PEI and plasmid GSDMD at different weight ratios, scale bar = 500 nm. (C) Diameter of NP_{GD}, NP_{FeS}, and $NP_{FeS/GD}$. (D) TEM and mapping analysis of NP_{FeS}, and $NP_{FeS/GD}$. The properties of released (E) Fe^{2+} and (F) H_2S of $NP_{FeS/GD}$ at pH 7.4 and 6.8. (G) CLSM observation of cellular uptake of $NP_{FeS/GD\text{-}Cy5}$, scale bar = 20 μm. (H) Quantification analysis of Cy5 signals in tumor cells as shown in (B). (I) The content of Fe in tumor cells after incubation with different time. (J) Intracellular H_2S generation of 4T1 cells incubated with NP_{GD}, NP_{FeS}, and $NP_{FeS/GD}$, scale bar = 100 μm.

4, 8, and 12 h). The results showed a time-dependent increase in Fe content, with the highest amount detected at 12 h of incubation (Fig. 2I). Furthermore, the generated H_2S from intracellular $NP_{FeS/GD}$ was measured using the WSP-1 method. As shown in Fig. 2J and Supporting Information Fig. S7, the green signal was observed in the NP_{FeS} and $NP_{FeS/GD}$ groups after incubation with cells for 4 h, while the other groups showed a low signal. This demonstrated that NP_{FeS} and $NP_{FeS/GD}$ could effectively release H_2S in tumor cells. These results suggested that the bioactive $NP_{FeS/GD}$ exhibited efficient cellular uptake and effectively released Fe^{2+} and H_2S intracellularly, making it a promising nanoplatform for targeted cancer therapy.

3.2. In vitro evaluation of $NP_{FeS/GD}$ -induced immunogenic panoptosis and ferroptosis cell death

Based on the design, the nanocomplex $NP_{FeS/GD}$ could trigger necrosis and apoptosis by generating H_2S at the tumor site, causing a redox imbalance and increasing ROS. It could also induce pyroptosis by the nanocomplex $NP_{FeS/GD}$-mediated GSDMD expression, leading to PANoptotic cell death of tumors. Firstly, intracellular ROS generation was also detected. The cells treated with NP_{FeS} and $NP_{FeS/GD}$ showed a stronger green signal after 12 h incubation than the groups treated with PBS and NP_{GD}, indicating that H_2S release could effectively induce a redox imbalance and increase ROS

(Supporting Information Fig. S8). To verify the activation of PANoptosis, the cells were stained with the Apoptosis and Necrosis Detection Kit (YO-PRO-1 and PI, YP1/PI) after co-incubation for 12 h. Apoptotic cells exhibited green fluorescence (YP1), while necroptotic cells displayed either red (PI) or green fluorescence (YP1). Pyroptotic cells were characterized by red fluorescence (PI), whereas PANoptotic cells emitted yellow fluorescence (YP1/PI). In Fig. 3A, cells exposed to $NP_{FeS/GD}$ displayed significantly higher levels of green and red fluorescence signals compared to the other groups, indicating an increase in the fractions of dead cell encompassing YO-PRO-1-positive cells (indicative of necroptosis or apoptosis) and PI-positive cells (indicative of pyroptosis or necroptosis). In addition, the cell viability of the normal human hepatocyte line (LO2) and the 4T1 tumor cells was measured after various treatments. Due to the lack of tumor-targeting ability, $NP_{FeS/GD}$ could also cause minimal damage to the normal cells of LO2. In contrast, tumor cells demonstrated increased malignancy, faster reproduction rates, and stronger phagocytosis ability, contributing to a more significant killing effect of nanomedicines on 4T1 tumor cells (Supporting Information Fig. S9). The expression levels of key proteins involved in the pyroptotic pathway (GSDMD), apoptotic pathway (caspase-3), and necroptotic pathway (phosphor mixed-lineage kinase domain-like, *p*-MLKL) were assessed following various treatments using confocal laser scanning microscopy (CLSM) and immunoblot analysis. The expression levels of GSDMD, caspase-3, and *p*-MLKL were significantly increased in 4T1 cells treated with $NP_{FeS/GD}$ compared to the control groups in CLSM imaging (Fig. 3B). The MFI of GSDMD indicated a significant increase in expression levels in the $NP_{FeS/GD}$-treated group, showing a 1.55- and 1.66-fold higher expression compared to the NP_{GD}-treated group and the NP_{FeS}-treated group, respectively (Supporting Information Fig. S10A). An increase in expression levels of caspase-3 and *p*-MLKL was significantly observed in the $NP_{FeS/GD}$ treated group, as indicated by the MFI (Fig. S10B and S10C). Immunoblot analysis revealed consistent findings regarding the increased expression of caspase-3 and GSDMD in cells treated with $NP_{FeS/GD}$ compared to other groups. Additionally, a notable increase in the expression of the necroptotic protein *p*-MLKL was observed in the $NP_{FeS/GD}$ group in comparison to the PBS group (Fig. 3C and Supporting Information Fig. S11). Furthermore, the expression levels of other key molecules implicated in PANoptosis, such as AIM2, ZBP1, and RIPK1, were measured *in vitro*. As illustrated in Supporting Information Fig. S12, a decline in the expression levels of AIM2, ZBP1, and RIPK1 was detected *via* immunoblot analysis, suggesting that $NP_{FeS/GD}$ treatment elicited AIM2, ZBP1, and RIPK1-dependent PANoptosis in tumor cells. The findings indicated that cells exposed to $NP_{FeS/GD}$ might induce PANoptotic cell death through the coordinated activation of necroptotic, apoptotic, and pyroptotic pathways. Due to the incorporation of FeS in the nanocomplex $NP_{FeS/GD}$ and NP_{FeS}, it could accumulate Fe^{2+} intracellularly, potentially triggering an alternative pathway to immunogenic cell death known as ferroptosis. The level of ferroptosis-related protein GPX4 was measured using Western blotting after treatment in 4T1 cells. The Western blot analysis revealed a reduced expression of GPX4 in cells treated with $NP_{FeS/GD}$ or NP_{FeS}, suggesting the partial induction of ferroptosis (Fig. 3D and Supporting Information Fig. S13). To further confirm ferroptosis, lipid peroxidation was measured using flow cytometry after treatment in 4T1 cells. The flow cytometry results and MFI measurements demonstrated a significant increase in lipid peroxidation in cells treated with $NP_{FeS/GD}$ compared to the control groups, indicating the initiation of ferroptosis (Fig. 3E and F). The transcriptome sequencing results of the PBS group and $NP_{FeS/GD}$ group revealed that differentially expressed genes were abnormally abundant in signaling pathways related to PANoptosis (pyroptosis, necroptosis, apoptosis), ferroptosis, and immune response regulation,

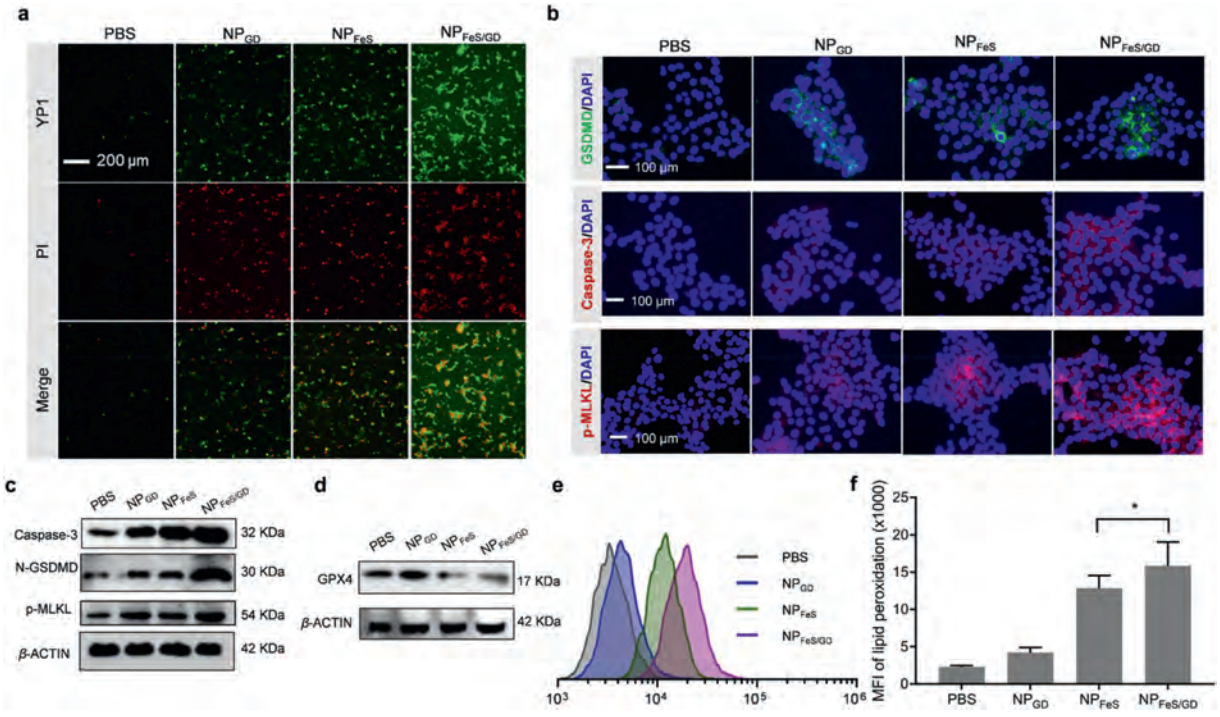

Figure 3 (A) YP1/PI analysis in 4T1 cells, scale bar = 200 μm. (B) CLSM imaging and (C) immunoblot analysis of GSDMD, caspase-3, and *p*-MLKL expression in 4T1 cells, scale bar = 100 μm. (D) GPX4 expression in 4T1 cells. The properties of released (E) FACS analysis and (F) MFI of lipid peroxidation in 4T1 cells. Data are shown as the mean ± SD ($n = 3$), $^*P < 0.05$.

further demonstrating the potential of PANoptosis in tumor immune sensitization therapy (Supporting Information Figs. S14−S16). To verify the contribution of each role in pyroptosis, necroptosis, apoptosis, and ferroptosis, the GSDMD inhibitor LDC7559, the apoptosis inhibitor Z-VAD-FMK, the necroptosis inhibitor Necrostatin-1, and the ferroptosis inhibitor Ferrostatin-1 were added to cells with different formulations to detect cell viability using Cell-Counting-Kit-8. As shown in Supporting Information Fig. S17, there was a 46.3% reduction in cell viability after cells were treated with Ferrostatin-1 and $NP_{FeS/GD}$, demonstrating that PANoptosis could damage cells more effectively. The cell viability was reduced by 65.6% after treatment with LDC7559, Z-VAD-FMK, Necrostatin-1, and $NP_{FeS/GD}$. Additionally, the cells treated with $NP_{FeS}/_{GD}$ showed a significantly greater inhibition with an 87.6% reduction. The coefficient of drug interaction[56] for PANoptosis and ferroptosis was 0.677, indicating a significant synergistic effect. The findings indicated that $NP_{FeS/GD}$ could effectively activate multiple immunogenic PANoptosis and ferroptosis cell death pathways simultaneously, offering a multi-faceted strategy for inducing cell death. This approach may enhance the efficacy of cancer cell treatment and mitigate the risk of resistance development.

3.3. *In vitro assessment of $NP_{FeS/GD}$-induced immune activation*

To verify the potential of $NP_{FeS/GD}$ to enhance the induction of immunogenic cell death (ICD) across multiple immunogenic PANoptosis and ferroptosis cell death pathways *in vitro*, the presence of danger-associated molecular patterns (DAMPs) such as high mobility group box 1(HMGB1), adenosine triphosphate (ATP) and the exposure of calreticulin (CRT) were investigated after treatment. Following treatment with different formulations, immunofluorescence staining was employed to measure the release of HMGB1 and the exposure of CRT. As shown in Fig. 4A, $NP_{FeS/GD}$ resulted in a substantial extracellular release of HMGB1 post-treatment. Moreover, $NP_{FeS/GD}$ effectively decreased HMGB1 levels by 64.6% and reduced positive staining of HMGB1 in the cell nucleus (Fig. 4B). A notable presence of CRT was identified on the surface of 4T1 cells following treatment with $NP_{FeS/GD}$ in Fig. 4C, with consistent findings corroborated through MFI analysis in Fig. 4D. The results indicated efficient extracellular release of HMGB1 and exposure of CRT in 4T1 cells. The ATP assay kit was used to assess ATP secretion, measuring extracellular ATP levels in 4T1 cells as an additional indicator of ICD. The results showed that ATP levels in the $NP_{FeS/GD}$ group were significantly higher than those in the PBS, $NP_{GD,}$ and NP_{FeS} groups (Fig. 4E). A noticeable decrease in HMGB1 expression, an increase in CRT expression, and enhanced ATP secretion were observed after treatment with $NP_{FeS/GD}$, providing evidence of a strong ICD response in tumor cells for triggering a subsequent immune response.

However, previous studies had shown that H_2S could downregulate IDO1 expression by blocking the NF-κB and STAT3 pathways, inhibiting IDO1 activity through H_2S/NO crosstalk, inducing the differentiation of cytotoxic T-effector cells and inhibiting MDSCs, effective inhibiting tumor development[53]. To further confirm whether the H_2S generated by $NP_{FeS/GD}$ could inhibit IDO expression and reverse the immunosuppressive microenvironment, we measured the accumulation of kynurenine (Kyn), a byproduct of IDO1 catalyzed tryptophan (Trp) consumption, as previously reported[57]. As shown in Supporting Information Fig. S18, the Kyn generation of $NP_{FeS/GD}$ and NP_{FeS} was lower than that of NP_{GD}, indicating that the production of H_2S inhibited the function of IDO1. The expression of IDO1 in cells was detected by immunofluorescence staining after different treatments. As shown in Fig. 4F and Supporting Information Fig. S19, it was demonstrated that IDO1 expression was regulated by the STAT3 and NF-κB pathways and that treatment with $NP_{FeS/GD}$ or NP_{FeS} could downregulate NF-κB phosphorylation and STAT3 phosphorylation to reduce the protein and mRNA expression levels of IDO1. As depicted in Fig. 4G and H, the expression of IDO1 in cells treated with $NP_{FeS/GD}$ or NP_{FeS} was comparable to that in the control group treated with PBS but lower than in the NP_{GD} group. This suggests that the released H_2S effectively reduces immune suppression by downregulating the expression of IDO1 *via* the STAT3 and NF-κB pathways (Fig. 4I). Hence, the experimental findings presented above offer compelling evidence that the nanocomplex $NP_{FeS/GD}$ was capable of inducing strong ICD and alleviating immune suppression.

Additionally, we investigated whether ICD triggered by multiple immunogenic PANoptosis and ferroptosis cell deaths could activate an innate immune response by releasing DAMPs that signal "eat me" to antigen-presenting cells (APCs), leading to the maturation and activation of dendritic cells (DCs). After the mouse bone marrow-derived dendritic cells (BMDCs) were incubated with 4T1 cells treated with PBS, NP_{GD}, NP_{FeS}, and $NP_{FeS/GD}$, the percentage of mature DCs was measured by flow cytometry. The results of FACS analysis revealed a significant increase in the expression of costimulatory molecules (CD80 and CD86) in BMDCs following treatment with $NP_{FeS/GD}$ during co-incubation (Fig. 4J). The $NP_{FeS/GD}$-treated group exhibited a 65.9% induction of mature DCs, representing a 2.11- and 1.83-fold increase compared to the NP_{GD}-treated group and NP_{FeS}-treated group, respectively. These results indicated that treatment with $NP_{FeS/GD}$ could enhance the activation and maturation of DCs (Fig. 4K). Consequently, the nanocomplex $NP_{FeS/GD}$ could trigger CRT exposure on the surface of tumor cells, enhance the extracellular release of HMGB1 and ATP, reduce the expression of IDO1, and thereby initiate ICD responses, leading to DC maturation and the initiation of anti-tumor immune responses.

3.4. *In vivo assessment of $NP_{FeS/GD}$-induced immune activation*

Before evaluating the immune activation and anti-tumor capability of $NP_{FeS/GD}$ to enhance the immune response *in vivo*, its biodistribution and tumor accumulation were investigated. Following intravenous injection of $NP_{FeS/GD\text{-}Cy5}$, the 4T1 tumor-bearing mice were analyzed using an IVIS (In Vivo Imaging System) instrument to track their fluorescence signal *via* the method in the previous study[58]. As shown in Fig. 5A and B, the Cy5 signal was still detectable in the serum after 48 h of $NP_{FeS/GD\text{-}Cy5}$ injection, indicating that $NP_{FeS/GD}$ exhibited a long circulation time and providing evidence for high enrichment in tumors. After systemic administration of $NP_{FeS/GD\text{-}Cy5}$, the tumoral Cy5 signal intensity gradually increased within 12 h and then gradually decayed after 12 h, demonstrating effective retention and accumulation of $NP_{FeS/GD}$ in tumors. The fluorescent signal of Cy5 in tumors was much higher than in other organs, confirming the outstanding capability of $NP_{FeS/GD}$ to be retained and accumulated in tumors (Fig. 5C and D). We also investigated the pharmacokinetics and biodistribution of free Cy5 in tumor-bearing mice with intravenous injection through the tail vein. As shown in Supporting Information Fig. S20, the free Cy5 decreased rapidly in the blood after 2 h of injection and disappeared at 12 h. In contrast, the fluorescence of $NP_{FeS/GD}$ remained after 48 h injection. The accumulation of free Cy5 in the tumor was further measured with *in vivo* imaging. After intravenous injection, a

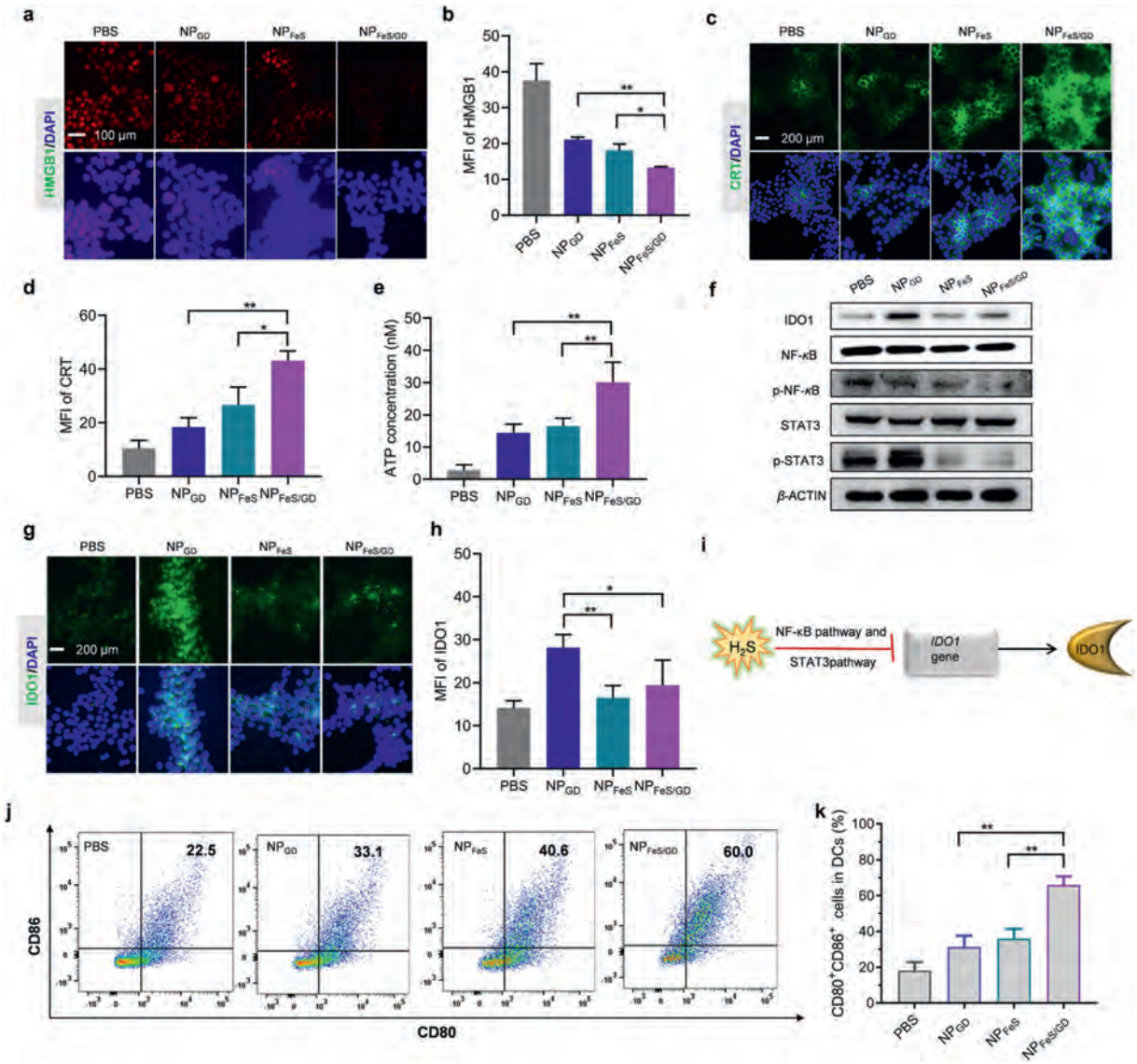

Figure 4 (A) CLSM images and (B) MFI of HMGB1 release in tumor cells, scale bar = 100 μm. (C) CLSM images and (D) MFI of CRT exposure in tumor cells, scale bar = 200 μm. (E) ATP secretion in supernatant after tumor cells treated. (F) IDO1 expression and related protein expression of NF-κB and STAT3 pathways in 4T1 cells. (G) CLSM images and (H) MFI of IDO1 expression in tumor cells, scale bar = 200 μm. (I) Schematic diagram depicting the modulation of H_2S on IDO1. (J) FACS plots and (K) analysis of the percentage of mature DCs after different treatments. Data are shown as the mean ± SD (n = 3), *P < 0.05, **P < 0.01.

lower fluorescence signal of Cy5 was observed at 4 h post-injection of free Cy5. The biodistribution and tumor accumulation study further supported the potential of $NP_{FeS/GD}$ as a promising candidate for immune activation in cancer therapy.

After confirming the tumor accumulation and retention of $NP_{FeS/GD}$, we assessed its capacity to induce immunogenic PANoptosis and ferroptosis cell death *in vivo*. 4T1 tumor-bearing mice were intravenously administered with PBS, NP_{GD}, NP_{FeS}, and $NP_{FeS/GD}$ at a plasmid dosage of 2 mg/kg. After 48 h, the tumors were harvested to prepare frozen tissue sections for further analysis. Subsequently, to confirm the PANoptosis, the expression of GSDMD, caspase-3, and *p*-MLKL in tumor tissues from the different groups was assessed through immunofluorescent staining. The $NP_{FeS/GD}$ treatment group showed a significant increase in PANoptosis proteins GSDMD, caspase-3, and p-MLKL, consistent with cellular-level observations (Fig. 5E). The results also reinforced the capacity of $NP_{FeS/GD}$ to trigger PANoptosis in tumors. Additionally, the levels of CRT and HMGB1, two key markers of ICD, were measured in the tumor tissues. The images showed a notable increase in CRT exposure and HMGB1 release in the tumor microenvironment of the $NP_{FeS/GD}$ group. The expression of IDO-1, as an immunosuppressive factor in the tumor microenvironment, was also measured using immunofluorescent staining. The observed downregulation of IDO-1 expression suggested that $NP_{FeS/GD}$ could effectively induce ICD in tumor cells and reverse immunosuppression *in vivo* (Fig. 5F). As shown in Supporting Information Fig. S21, the content of Trp in tumors treated with $NP_{FeS/GD}$ and NP_{FeS} was higher than that in the NP_{GD} group, indicating their potential to enhance T-cell responses. Meanwhile, the pro-inflammatory cytokines IL-6, TNF-α, and IFN-γ were detected in the serum at 48 h post-virous treatments. Following $NP_{FeS/GD}$ treatment, higher levels of TNF-α, IL-6, and

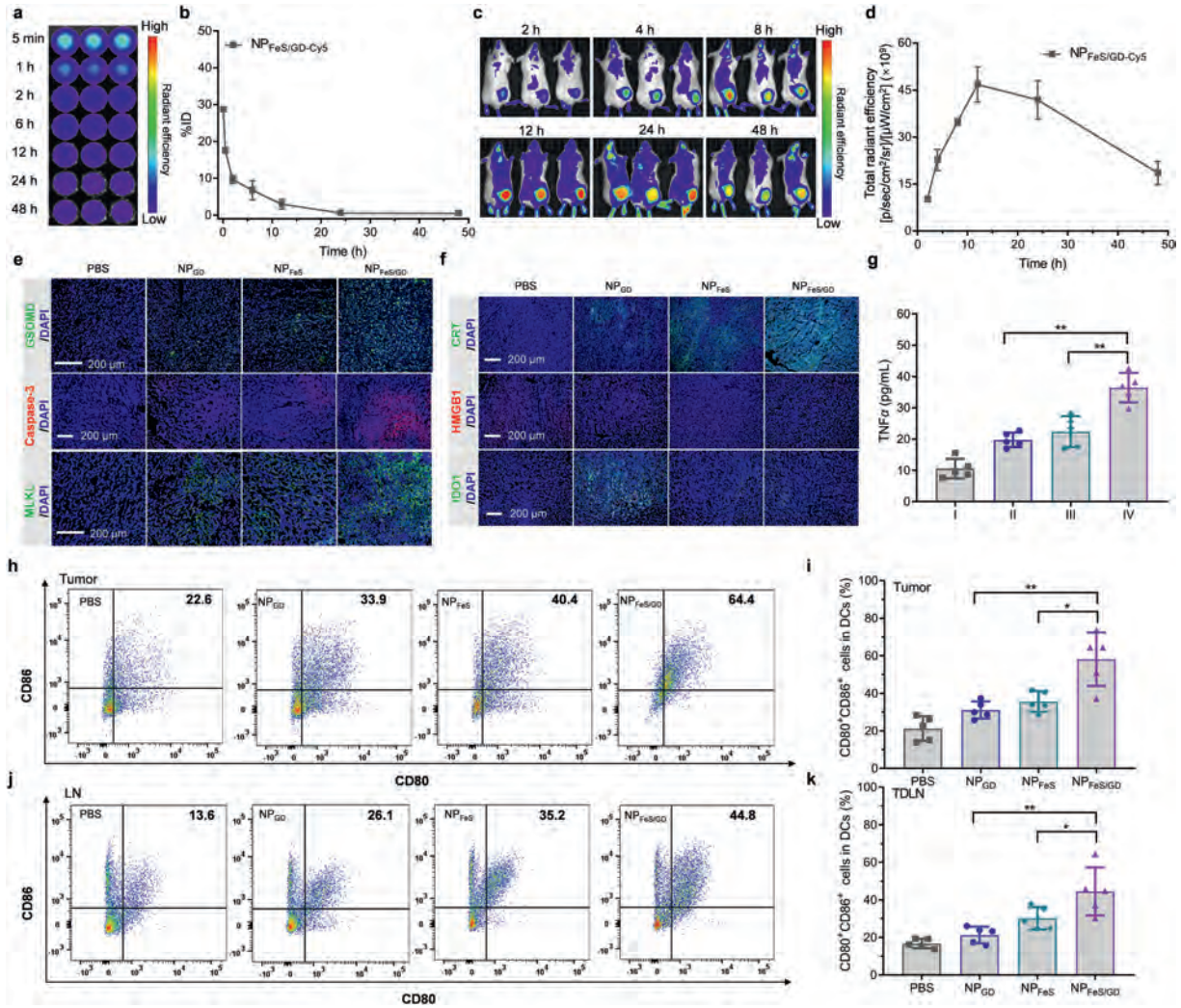

Figure 5 (A) The images and (B) analysis of pharmacokinetics after $NP_{FeS/GD\text{-}Cy5}$ treated. (C) The images and (D) analysis of tumor accumulation after $NP_{FeS/GD\text{-}Cy5}$ treated. (E) CLSM images of expression of GSDMD, caspase-3, and *p*-MLKL in tumor section, scale bar = 200 μm. (F) CLSM images of expression of CRT, HMGB1, and IDO1 in tumor, scale bar = 200 μm. (G) The content of TNFα in serum. FACS plots and analysis of the percentage of mature DCs in tumor (H, I) and TDLN (J, K) after different treatments. Data are shown as the mean ± SD ($n = 5$), $^*P < 0.05$, $^{**}P < 0.01$.

IFN-γ cytokines were observed at the 48 h mark compared to the other groups (Fig. 5G and Supporting Information Fig. S22). To validate the immune activation of $NP_{FeS/GD}$, tumor-bearing mice were intravenously injected with PBS, NP_{GD}, NP_{FeS}, and $NP_{FeS/GD}$ at a plasmid dosage of 2 mg/kg. Subsequently, the activation of DCs in tumors and tumor-draining lymph nodes was assessed using flow cytometry post-treatment. The $NP_{FeS/GD}$-treatment group demonstrated a significantly higher proportion of mature DCs (58.1%) compared to the PBS group (21.2%), indicating a 2.74-fold increase (Fig. 5H and I). The proportion of M1-type macrophages ($CD86^+CD11b^+F4/80^+$) within tumor tissues was measured. As depicted in Supporting Information Fig. S23, the percentage of CD86-positive $CD11b^+F4/80^+$ macrophages (M1-type macrophages) was 36.2% after PBS treatment, which increased to 64.5% after $NP_{FeS/GD}$ treatment. The results indicated that $NP_{FeS/GD}$ treatment effectively triggers an immune response by promoting DC maturation and M1-type macrophage polarization. Moreover, the percentage of mature DCs (44.5%) observed in tumor-draining lymph nodes (TDLN) after $NP_{FeS/GD}$ treatment surpassed that of all other groups (Fig. 5J and K). The $NP_{FeS/GD}$ compound could trigger robust immunogenic cell death, leading to the release of DAMPs and depletion of IDO-1. The process induces an immune response by stimulating DC maturation and increasing cytokine expression, leading to the activation of anti-tumor immunity and the reversal of tumor immunosuppression.

3.5. *Tumor immunotherapy of $NP_{FeS/GD}$ in vivo*

After demonstrating the efficient immune activation effect *in vivo* mediated by $NP_{FeS/GD}$, the subsequent evaluation focuses on the antitumor therapy effect. Female Balb/C mice were subcutaneously implanted with 4T1 cells on the left side and then randomly allocated tumor-bearing mice into treatment groups. The *in vivo* antitumor investigation comprised the systemic administration of treatment formulations on Days 3, 6, and 9, with monitoring every 3 days for 15 days post-injection. The mice treated with NP_{GD} (Group II) and NP_{FeS} (Group III) showed a 35.5% and 48.2% inhibition of tumor growth, respectively, compared to the PBS group (Group I). $NP_{FeS/GD}$ (Group IV) showed significantly greater inhibition of tumors compared to the NP_{FeS} and NP_{GD} groups, as evidenced by an

82.2% reduction in tumor burden compared to the PBS group (Fig. 6A). Moreover, images of dissected tumor tissues from various treatment groups (Fig. 6B) and the tumor tissue mass (Fig. 6C) displayed a consistent pattern in tumor volume. The TUNEL apoptosis assay conducted on excised tumors further confirmed that $NP_{FeS/GD}$ exhibited the highest efficacy in suppressing tumor growth (Fig. 6D). Despite the various treatments administered during the therapeutic experiment, there was no significant decrease

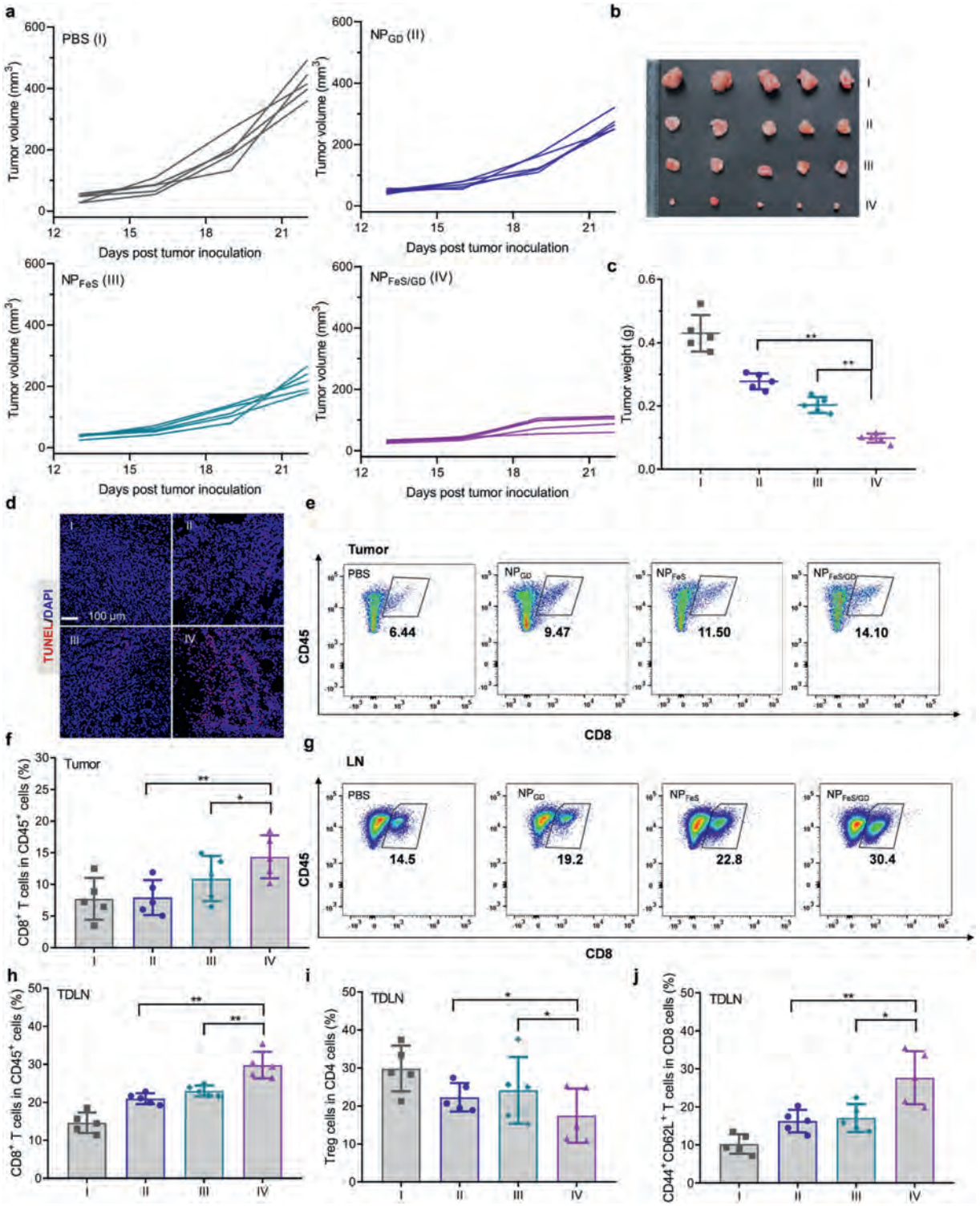

Figure 6 (A) The tumor inhibition curves after various treatments (PBS (Group I), NP_{GD} (Group II), NP_{FeS} (Group III), and $NP_{FeS/GD}$ (Group IV). (B) Images and (C) weight of tumors receiving various treatments. (D) The TUNEL stanning of tumor after various treatments treated, scale bar = 100 μm. (E) The FACS plots and (F) analysis of $CD8^+$ T cells in $CD45^+$ cells in tumor receiving various treatments. (G) The FACS plots and (H) analysis of $CD8^+$ T cells in TDLN receiving various treatments. The percentage of (I) Treg cells in CD4 cells and (J) $CD44^+CD62L^+$ T cells in CD8 cells in TDLN after treated with various treatments. Data are shown as the mean ± SD ($n = 5$), $^*P < 0.05$, $^{**}P < 0.01$.

in the body weight of the mice as monitored. The observation indicated a remarkable biosafety profile of the $NP_{FeS/GD}$ treatment (Supporting Information Fig. S24). Furthermore, the heart, liver, spleen, lung, and kidney were collected to assess their pathological condition by hematoxylin and eosin (HE) staining. As shown in Supporting Information Fig. S25, the tissue structures and cell morphology were visible. It was evident that there was minimal tissue damage in the major organs following treatment with various formulations. The data collectively confirmed the capability of the nanocomplex $NP_{FeS/GD}$ to inhibit tumor growth, induce tumor cell death, and show satisfactory safety.

For a more comprehensive insight into immune response mechanisms after different treatments *in vivo*, the percentage of immune cells in tumors and tumor-draining lymph nodes was assessed through flow cytometry (Supporting Information Fig. S26). The $NP_{FeS/GD}$-treated group displayed the most notable infiltration of cytotoxic $CD8^+$ T lymphocytes within tumor tissues (23.0%), aligning with its role in tumor suppression (Fig. 6E and F). A significant increase in cytotoxic $CD8^+$ T cells was observed in the tumor-draining lymph nodes following $NP_{FeS/GD}$ treatments compared to the other groups (Fig. 6G and H). As illustrated in Supporting Information Fig. S27, the proportion of $CD8^+$ T lymphocytes within the spleen was around 11.5% following $NP_{FeS/GD}$ treatment, exhibiting a notable increase compared to other groups. The results were aligned with those observed in tumors and tumor-draining lymph nodes, which collectively demonstrated that $NP_{FeS/GD}$ treatment could elicit systemic $CD8^+$ T cell antitumor immunity. Furthermore, there was a notable reduction in the proportion of regulatory T cells (Tregs), the primary immunosuppressive cells, in tumor-draining lymph nodes treated with $NP_{FeS/GD}$ (Fig. 6I and Supporting Information Fig. S28). The infiltration of central memory T cells within tumor-draining lymph nodes after $NP_{FeS/GD}$ treatment demonstrated a marked increase, indicating a durable immune memory response (Fig. 6J and Supporting Information Fig. S29). The results collectively demonstrated that the $NP_{FeS/GD}$ group effectively induced antitumor T cell immunity and reversed tumor immunosuppression.

3.6. $NP_{FeS/GD}$ suppresses tumor metastasis in vivo

Metastasis of breast cancer to the lung was a primary factor contributing to the ineffectiveness of traditional cancer therapies. Hence, it was imperative to assess the efficacy of $NP_{FeS/GD}$ in inhibiting 4T1 tumor metastasis. The aggressive whole-body 4T1 tumor metastasis model was established by intravenous injection of 4T1-luciferase tumor cells into BALB/c mice *via* the tail vein. Subsequently, the mice received intravenous injections of PBS (Group I), NP_{GD} (Group II), NP_{FeS} (Group III), and $NP_{FeS/GD}$

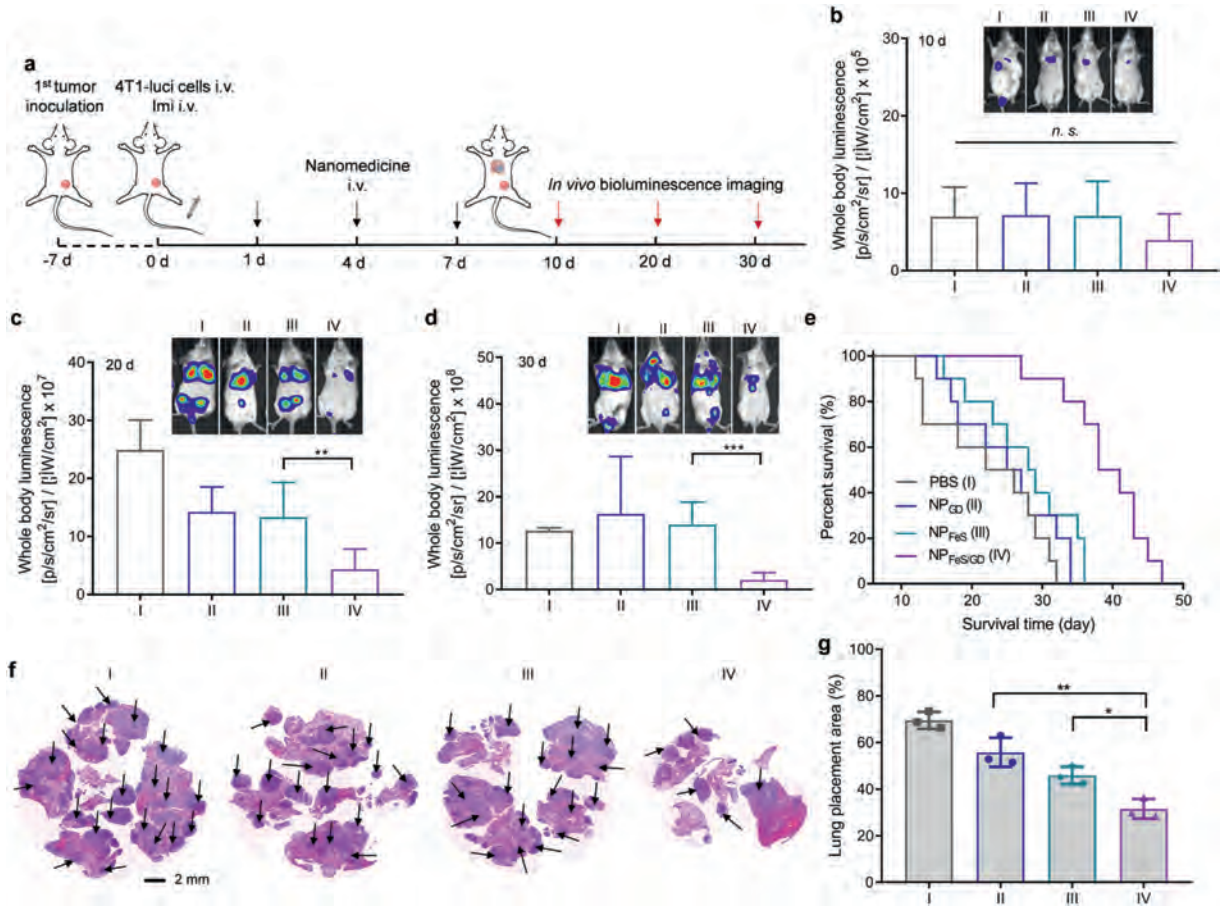

Figure 7 (A) Schematic illustration of treatment schedule against lung metastasis (PBS (Group I), NP_{GD} (Group II), NP_{FeS} (Group III), and $NP_{FeS/GD}$ (Group IV)). Typical *in vivo* bioluminescence images and corresponding quantifications of tumor burdens on (B) Day 10, (C) Day 20 and (D) Day 30. (E) Survival curves of mice received various treatments. (F) Representative HE stanning showing the metastatic nodules on the lung, scale bar = 2 mm. (G) The corresponding percentage of metastatic lung placement area receiving the various treatments. Data are shown as the mean ± SD ($n = 3$), $^*P < 0.05$, $^{**}P < 0.01$, $^{***}P < 0.001$, *n.s.*, not significant.

(Group IV) on Days 1, 4, and 7. Monitoring included assessment of whole-body luciferase expression and survival of the mice (Fig. 7A). The results showed that the $NP_{FeS/GD}$-treated group exhibited slightly lower whole-body luciferase expression compared to the other groups on Day 10 (Fig. 7B). On Days 20 and 30, there were a particularly obvious difference in decreased bioluminescence signals in mice treated with $NP_{FeS/GD}$ compared to NP_{GD} and NP_{FeS}, as evidenced by the effective suppression of metastasis (Fig. 7C and D). Additionally, the survival rate of the $NP_{FeS/GD}$-treated mice was significantly higher than that of the other groups. The treatments were continued for up to 47 days. The survival studies revealed a considerably extended animal survival, with 70% of mice in Group IV remaining alive-whereas all the mice died within 38 days in the other groups (Fig. 7E). Moreover, the bioluminescence signals and HE staining of entire lungs validated the anti-metastatic efficacy of $NP_{FeS/GD}$. Mice administered with $NP_{FeS/GD}$ displayed reduced luciferase activity in the lungs, and histological analysis of lung tissues revealed a significant reduction in the number and size of metastatic nodules in the $NP_{FeS/GD}$-treated group (Fig. 7F and G). These findings suggested that $NP_{FeS/GD}$ effectively suppresses breast cancer metastasis *in vivo*. Collectively, the results verified that the anti-tumor immune response induced by $NP_{FeS/GD}$ offers a promising approach for inhibiting tumor growth and suppressing metastasis.

4. Conclusions

In conclusion, bioactive $NP_{FeS/GD}$ has been successfully developed to simultaneously activate immunogenic PANoptosis and ferroptosis, utilizing H_2S amplification to remodel the immunosuppressive-sensitized tumor immunotherapy. The bioactive $NP_{FeS/GD}$ could release GSDMD plasmid, H_2S, and Fe^{2+} in response to the tumor microenvironment and elicit highly immunogenic PANoptosis and ferroptosis, effectively triggering the antitumor innate and adaptive immune responses. The release of H_2S could also relieve the over-expression of IDO1 caused by immunogenic PANoptosis and ferroptosis, inhibiting IDO1 activity and reversing the tumor immunosuppressive microenvironment to enhance antitumor immunotherapy. This study highlights the potential of immunogenic PANoptosis and ferroptosis in H_2S gas therapy as a strategy to reprogram the tumor immunosuppressive microenvironment, enhancing the effectiveness of immunotherapy and inhibiting metastasis.

Acknowledgments

This work was supported by the National Natural Science Foundation of China (52103164 and 82172073), the Yong Elite Scientist Sponsorship Program by CAST (No. YESS20200177, China), the Fundamental Research Funds for the Central Universities (JUSRP123079 and JUSRP123078, China), and the Guangdong Basic and Applied Basic Research Foundation (2021A1515220033, China).

Author contributions

Yingli Luo: Funding acquisition, Conceptualization. Maoyuan Linghu: Methodology, Data curation. Xianyu Luo: Methodology. Dongdong Li: Methodology. Jilong Wang: Methodology. Shaojun Peng: Writing − review & editing, Funding acquisition. Yinchu Ma: Writing − original draft, Methodology, Funding acquisition, Conceptualization.

Conflicts of interest

There are no conflicts of interest to declare.

Appendix A. Supporting information

Supporting information to this article can be found online at https://doi.org/10.1016/j.apsb.2024.12.014.

References

1. Dagher OK, Schwab RD, Brookens SK, Posey AD. Advances in cancer immunotherapies. *Cell* 2023;**186**:1814−5.
2. Wang DR, Wu XL, Sun YL. Therapeutic targets and biomarkers of tumor immunotherapy: response *vssersus* non-response. *Signal Transduct Tar Ther* 2022;**7**:331.
3. Zhang YY, Zhang ZM. The history and advances in cancer immunotherapy: understanding the characteristics of tumor-infiltrating immune cells and their therapeutic implications. *Cell Mol Immunol* 2020;**17**:807−21.
4. Kirchhammer N, Trefny MP, Maur PAD, Läubli H, Zippelius A. Combination cancer immunotherapies: emerging treatment strategies adapted to the tumor microenvironment. *Sci Transl Med* 2022;**14**: eabo3605.
5. Chen Y, Zhou Q, Jia Z, Cheng N, Zhang S, Chen W, et al. Enhancing cancer immunotherapy: nanotechnology-mediated immunotherapy overcoming immunosuppression. *Acta Pharm Sin B* 2024;**14**: 3834−54.
6. Martin JD, Cabral H, Stylianopoulos T, Jain RK. Improving cancer immunotherapy using nanomedicines: progress, opportunities and challenges. *Nat Rev Clin Oncol* 2020;**17**:251−66.
7. Fan T, Zhang MN, Yang JX, Zhu ZA, Cao WL, Dong CY. Therapeutic cancer vaccines: advancements, challenges, and prospects. *Signal Transduct Tar Ther* 2023;**8**:450.
8. Kubli SP, Berger T, Araujo DV, Siu LL, Mak TW. Beyond immune checkpoint blockade: emerging immunological strategies. *Nat Rev Drug Discov* 2021;**20**:899−919.
9. Tay C, Tanaka A, Sakaguchi S. Tumor-infiltrating regulatory T cells as targets of cancer immunotherapy. *Cancer Cell* 2023;**41**:450−65.
10. Xu H, Qin X, Guo Y, Zhao S, Feng X, Zhang R, et al. Radiation-based immunogenic vaccine combined with a macrophage "checkpoint inhibitor" for boosting innate and adaptive immunity against metastatic colon cancers. *Acta Pharm Sin B* 2024;**14**:2247−62.
11. Liu X, Liang S, Sang X, Chang L, Fu S, Yang H, et al. On-demand integrated nano-engager converting cold tumors to hot *via* increased DNA damage and dual immune checkpoint inhibition. *Acta Pharm Sin B* 2023;**13**:1740−54.
12. Jhunjhunwala S, Hammer C, Delamarre L. Antigen presentation in cancer: insights into tumour immunogenicity and immune evasion. *Nat Rev Cancer* 2021;**21**:298−312.
13. Tang TY, Huang X, Zhang G, Hong ZT, Bai XL, Liang TB. Advantages of targeting the tumor immune microenvironment over blocking immune checkpoint in cancer immunotherapy. *Signal Transduct Tar Ther* 2021;**6**:72.
14. Wang B, Zhao Q, Zhang YY, Liu ZJ, Zheng ZZ, Liu SY, et al. Targeting hypoxia in the tumor microenvironment: a potential strategy to improve cancer immunotherapy. *J Exp Clin Canc Res* 2021;**40**:1−16.
15. Peng SJ, Xiao FF, Chen MW, Gao HL. Tumor-microenvironment-responsive nanomedicine for enhanced cancer immunotherapy. *Adv Sci* 2022;**9**:2103836.
16. Lang F, Schrörs B, Löwer M, Türeci Ö, Sahin U. Identification of neoantigens for individualized therapeutic cancer vaccines. *Nat Rev Drug Discov* 2022;**21**:261−82.
17. Zhu SM, Zhang T, Zheng L, Liu HT, Song WR, Liu DL, et al. Combination strategies to maximize the benefits of cancer immunotherapy. *J Hematol Oncol* 2021;**14**:156.

18. Dai EY, Zhu Z, Wahed S, Qu ZX, Storkus WJ, Guo ZS. Epigenetic modulation of antitumor immunity for improved cancer immunotherapy. *Mol Cancer* 2021;**20**:1−27.
19. Zhou LQ, Lyu J, Liu F, Su YH, Feng L, Zhang XJ. Immunogenic PANoptosis-initiated cancer sono-immune reediting nanotherapy by iteratively boosting cancer immunity cycle. *Adv Mater* 2024;**36**:2305361.
20. Lin JF, Hu PS, Wang YY, Tan YT, Yu K, Liao K, et al. Phosphorylated NFS1 weakens oxaliplatin-based chemosensitivity of colorectal cancer by preventing PANoptosis. *Signal Transduct Tar Ther* 2022;**7**:54.
21. Xu XY, Shabiti S, Zhang X, Zheng JL, Liang N, Wang ZX, et al. Membrane-anchoring clickable Iridium(III) nanosonosensitizer *in situ* evokes PANoptosis for augmented tumor sono-immunotherapy. *Nano Today* 2024;**56**:102270.
22. Wu CY, Liu ZL, Chen ZX, Xu DL, Chen LS, Lin H, et al. A nonferrous ferroptosis-like strategy for antioxidant inhibition-synergized nanocatalytic tumor therapeutics. *Sci Adv* 2021;**7**:eabj8833.
23. Jiang XJ, Stockwell BR, Conrad M. Ferroptosis: mechanisms, biology and role in disease. *Nat Rev Mol Cell Bio* 2021;**22**:266−82.
24. Tang DL, Chen X, Kang R, Kroemer G. Ferroptosis: molecular mechanisms and health implications. *Cell Res* 2021;**31**:107−25.
25. von Krusenstiern AN, Robson RN, Qian NX, Qiu BY, Hu FH, Reznik E, et al. Identification of essential sites of lipid peroxidation in ferroptosis. *Nat Chem Biol* 2023;**19**:719−30.
26. Pandeya A, Kanneganti TD. Therapeutic potential of PANoptosis: innate sensors, inflammasomes, and RIPKs in PANoptosomes. *Trends Mol Med* 2024;**30**:74−88.
27. Sundaram B, Pandian N, Mall R, Wang YQ, Sarkar R, Kim HJ, et al. NLRP12-PANoptosome activates PANoptosis and pathology in response to heme and PAMPs. *Cell* 2023;**186**:2783−801.
28. Xue CC, Li MH, Zhao Y, Zhou J, Hu Y, Cai KY, et al. Tumor microenvironment-activatable Fe-doxorubicin preloaded amorphous $CaCO_3$ nanoformulation triggers ferroptosis in target tumor cells. *Sci Adv* 2020;**6**:eaax1346.
29. Li T, Kroemer G. Mechanisms of programmed cell death. *Immunol Rev* 2024;**321**:5−6.
30. Du FX, Zhao HX, Song YMH, Feng ZY, Liu K, Wang ZY, et al. Apoptosis-sensitizing tumor nanomedicine by regulating pyroptosis-associated inflammatory cell death. *Adv Funct Mater* 2024:2406150.
31. Cai M, Fu T, Zhu R, Hu P, Kong J, Liao S, et al. An iron-based metal-organic framework nanoplatform for enhanced ferroptosis and oridonin delivery as a comprehensive antitumor strategy. *Acta Pharm Sin B* 2024;**14**:4073−86.
32. Elzoghby AO, Samir O, Emam HE, Soliman A, Abdelgalil RM, Elmorshedy YM, et al. Engineering nanomedicines for immunogenic eradication of cancer cells: recent trends and synergistic approaches. *Acta Pharm Sin B* 2024;**14**:2475−504.
33. Kao AT, Cabanlong CV, Padilla K, Xue X. Unveiling ferroptosis as a promising therapeutic avenue for colorectal cancer and colitis treatment. *Acta Pharm Sin B* 2024;**14**:3785−801.
34. Gao Y, Song ZL, Yu S, Zhao XL, Chen DW, Qiao MX. Enhanced ferroptosis by a nanoparticle mimicking hemoglobin coordinate pattern with self-supplying hydrogen peroxide. *Chin Chem Lett* 2024:110097.
35. Li KH, Zhao HY, Wang DD, Qi MH, Xu ZJ, Li JM, et al. Mitochondria-targeted nano-AIEgens as a powerful inducer for evoking immunogenic cell death. *Chin Chem Lett* 2024;**35**:108882.
36. Elzoghby AO, Samir O, Emam HE, Soliman A, Abdelgalil RM, Elmorshedy YM, et al. Engineering nanomedicines for immunogenic eradication of cancer cells: recent trends and synergistic approaches. *Acta Pharm Sin B* 2024;**14**:2475−504.
37. Zhu L, Luo MY, Zhang YF, Fang F, Li M, An FF, et al. Free radical as a double-edged sword in disease: deriving strategic opportunities for nanotherapeutics. *Coordin Chem Rev* 2023;**475**:214875.
38. Zhang Y, Fang C, Zhang W, Zhang K. Emerging pyroptosis-engineered nanobiotechnologies regulate cancers and inflammatory diseases: a double-edged sword. *Matter* 2022;**5**:3740−74.
39. Mardi A, Shirokova AV, Mohammed RN, Keshavarz A, Zekiy AO, Thangavelu L, et al. Biological causes of immunogenic cancer cell death (ICD) and anti-tumor therapy; combination of oncolytic virus-based immunotherapy and CAR T-cell therapy for ICD induction. *Cancer Cell Int* 2022;**22**:168.
40. Li QL, Liu J, Fan HL, Shi L, Deng Y, Zhao L, et al. IDO-inhibitor potentiated immunogenic chemotherapy abolishes primary tumor growth and eradicates metastatic lesions by targeting distinct compartments within tumor microenvironment. *Biomaterials* 2021;**269**:120388.
41. Yang Z, Gao D, Guo XQ, Jin L, Zheng JJ, Wang Y, et al. Fighting immune cold and reprogramming immunosuppressive tumor microenvironment with red blood cell membrane-camouflaged nanobullets. *Acs Nano* 2020;**14**:17442−57.
42. Huang P, Yang Y, Wang WY, Li ZM, Gao NS, Chen HZ, et al. Self-driven nanoprodrug platform with enhanced ferroptosis for synergistic photothermal-IDO immunotherapy. *Biomaterials* 2023;**299**.
43. Guo YX, Liu Y, Wu W, Ling DS, Zhang Q, Zhao P, et al. Indoleamine 2,3-dioxygenase (Ido) inhibitors and their nanomedicines for cancer immunotherapy. *Biomaterials* 2021;**276**:122157.
44. Kim M, Lee JS, Kim W, Lee JH, Jun BH, Kim KS, et al. Aptamer-conjugated nano-liposome for immunogenic chemotherapy with reversal of immunosuppression. *J Control Release* 2022;**348**:893−910.
45. Feng XR, Xu WG, Liu JH, Li D, Li G, Ding JX, et al. Polypeptide nanoformulation-induced immunogenic cell death and remission of immunosuppression for enhanced chemoimmunotherapy. *Sci Bull* 2021;**66**:362−73.
46. Guo Q, Xu X, Lai X, Duan J, Yan D, Wang D. Antigen/adjuvant-free liposome induces adjuvant effects for enhancing cancer immunotherapy. *Exploration* 2024:20230115.
47. Cirino G, Szabo C, Papapetropoulos A. Physiological roles of hydrogen sulfide in mammalian cells, tissues, and organs. *Physiol Rev* 2023;**103**:31−276.
48. Lin HC, Yu YX, Zhu L, Lai NN, Zhang LM, Guo Y, et al. Implications of hydrogen sulfide in colorectal cancer: mechanistic insights and diagnostic and therapeutic strategies. *Redox Biol* 2023;**59**:102601.
49. Yue TH, Li JC, Zhu J, Zuo S, Wang X, Liu YC, et al. Hydrogen sulfide creates a favorable immune microenvironment for colon cancer. *Cancer Res* 2023;**83**:595−612.
50. Sun WY, Zhu CY, Song J, Ji SC, Jiang BP, Liang H, et al. Hydrogen sulfide gas amplified ROS cascade: FeS@GOx hybrid nanozyme designed for boosting tumor chemodynamic immunotherapy. *Adv Healthc Mater* 2023;**12**:2300385.
51. Liu L, Lei HL, Hou GH, Zhang L, Chen YD, Lu YJ, et al. Gas-amplified metalloimmunotherapy with dual activation of pyroptosis and the sting pathway for remodeling the immunosuppressive cervical cancer microenvironment. *Acs Nano* 2024;**18**:12830−44.
52. Li Z, Chu ZY, Yang J, Qian HS, Xu JM, Chen BJ, et al. Immunogenic cell death augmented by manganese zinc sulfide nanoparticles for metastatic melanoma immunotherapy. *Acs Nano* 2022;**16**:15471−83.
53. Yang D, Li T, Li Y, Zhang S, Li W, Liang H, et al. H_2S suppresses indoleamine 2, 3-dioxygenase 1 and exhibits immunotherapeutic efficacy in murine hepatocellular carcinoma. *J Exp Clin Canc Res* 2019;**38**:1−15.
54. Yu L, Lu J, Du WB. Tryptophan metabolism in digestive system tumors: unraveling the pathways and implications. *Cell Commun Signal* 2024;**22**:174.
55. Liu H, Mu MY, Hou YB, Gong YF, Wang CY, Ma GQ, et al. A novel CRISPR/Cas9-encapsulated biomimetic manganese sulfide nanourchins for targeted magnetic resonance contrast enhancement and self-enhanced chemodynamics-gene-immune synergistic tumor therapy. *Adv Funct Mater* 2024;**24**:2401370.
56. Hou S, Li Z, Chen X, Wang W, Duan T, Scampavia L, et al. Elemene sensitizes pancreatic cancer cells to bortezomib by enhancing proteasome inhibition *via* molecular patch mechanism. *Signal Transduct Tar Ther* 2023;**8**:87.
57. Li Z, Pei Q, Zhao M, Xie Z, Zheng M. Self-carrier nanoparticles for delivery of paclitaxel and IDO inhibitor to boost antitumor chemo-immunotherapy. *Adv Funct Mater* 2024:2312500.
58. Wang Q, Liang QR, Dou JX, Zhou H, Zeng CC, Pan HM, et al. Breaking through the basement membrane barrier to improve nanotherapeutic delivery to tumours. *Nat Nanotechnol* 2024;**19**:95−105.